Chapter 1

A Brief Overview of Some Cosmic Ray Measurements

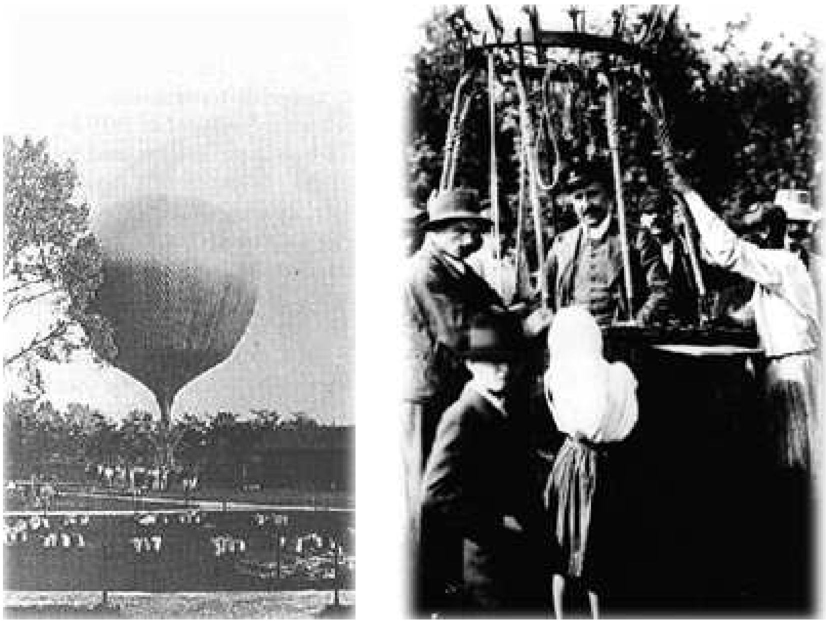

Figure 1.1: Balloon flights of Victor Hess.

> “The results of my observations are best explained by the assumption that a radiation of very great penetrating power enters our atmosphere from above”
>
> Victor Hess, Physikalische Zeitschrift, November 1912

The history of cosmic rays started with a very simple instrument - the electroscope. By the end of the 19th century it was known that electroscopes discharged spontaneously due to the ionization of the air, and the rate of discharge of the instrument allowed to quantify this effect. The cause of air ionization was believed to be the natural radioactivity of the Earth. It should therefore decrease with the distance to ground. Several meaurements were conducted to determine the rate of discharge with altitude, the most famous being the one performed by Thomas Wulf in 1910, in which he took an electroscope to the top of the Eiffel tower. The results showed that the rate of discharge did not decrease as fast as it was expected. In 1912 Victor Hess flew this kind of instrument in hot air balloons to measure the rate of air ionization with altitude. Hess was able to fly and perform measurements up to an altitude of 5 km. The results showed that the ionization rate decreased from ground level to ~ 1 km and then increased with altitude. Such a decrease proved that in fact a part of the air ionization effect was due to the natural radioactivity of the Earth. The subsequent increase in the rate, and thus in the air ionization effect, was attributed by Hess to some kind of radiation arriving to Earth from Space. The quest to measure such radiation went further with the development of automatic data acquisition systems for the electroscopes. The devices were then used in unmanned balloon flights that could reach higher altitudes. Such flights would confirm Hess results and, eventually, in 1926, Robert Millikan coined the term “Cosmic Rays” to describe these phenomena.

More sophisticated instruments for the detection of radiation became available and started to be used in the cosmic ray field. Such instruments, like the cloud chamber and photographic emulsions, allowed particle tracks to be recorded and, by the use of magnetic fields, to extract particle parameters like their mass and charge. In this context particle physics was born, with the discovery of new particles: the positron in 1932, the muon in 1937, the pion in 1947 followed by the discovery of “strange” particles.

By the mid 1930s, counters in coincidence were being used in the study of cosmic rays. At this point an excess in the coincidence rate suggested that particles arrived in bunches. Later, with the the development of coincidence units with better timing resolution (around 5 microseconds), Pierre Auger was able to conduct systematic studies and establish the occurrence of air showers. The discovery of Extensive Air Showers (EAS) was a breakthrough as it allowed a correlation between the particles detected at ground and high energy cosmic particles reaching the top of the atmosphere to be established, and to go higher in energy by building ever larger sampling detectors. The path to the study of highly energetic cosmic rays was opened. Still today, sampling detectors are widely used to detect cosmic rays with an energy up to $\sim 10^{20}$ eV with very large sampling arrays. The largest one, the Pierre Auger Observatory, has an area of $\sim 3000\,\mathrm{km}^2$.

An alternative technique to detect EAS - the fluorescence technique - was meanwhile developed. The first studies to detect fluorescence in the atmosphere were performed in the early 1960s in the Los Alamos National Laboratory for military purposes related with nuclear explosions. The idea to use the technique to detect cosmic rays was first proposed by the Cornell Cosmic Ray Observatory in the mid 1960s but was unsuccessful as it was not able to detect light from EAS. The first successful observation of fluorescence light from EAS would come in 1976 with the installation of prototype telescopes in Volcano Ranch by physicist from the Utah University. In 1981 Fly's Eye becomes the first cosmic ray experiment employing the fluorescence technique, which is a well-established technique nowadays. The Pierre Auger Observatory uses this technique together with the sampling technique. The hybrid detection capabilities are one of the strengths of the Observatory, allowing the cross-calibration of the two methods and reducing the systematic errors.

High energy γ-rays have energies in the GeV - TeV range and originate pure electromagnetic showers. Such showers develop high in the atmosphere, making the detection of the front of particles at ground impossible. Also, the fluorescence light emitted by such low energy showers falls below the sensitivity of fluorescence detectors. However, the shower development produces Cherenkov light that accumulates and propagates along the shower direction, producing a signal detectable at ground. In the late 1960s the programme to study the Cherenkov light emitted by EAS started with the Whipple observatory. The idea was to record this light by mean of telescopes. The background from charged cosmic rays was however enormous. The method became more efficient with the introduction of imaging techniques (Hillas, 1985), in which segmented focal surfaces and shower shape variables allowed to distinguish showers initiated by energetic gamma rays. In recent years, larger telescopes and telescope arrays were built, allowing the discovery of an impressive number of γ-ray sources in the sky. Most of the recent results have been provided by HESS, installed in Namibia, and the MAGIC telescope, in the Canary islands.

1.1 Cosmic rays flux

The energy spectrum of cosmic rays covers a very wide range both in energy and flux. In figure 1.2 the differential flux multiplied by E^2 as a function of the energy

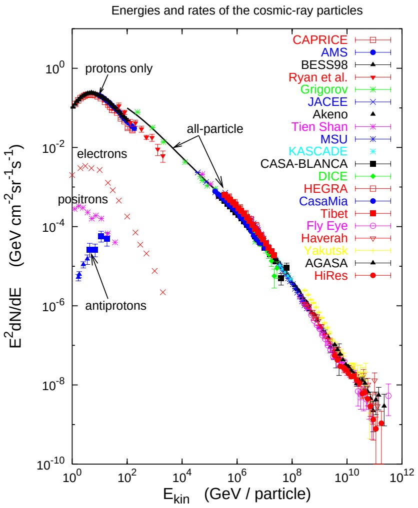

Figure 1.2: Energy spectrum of Cosmic Rays. The differential flux multiplied by E^2 is plotted against the energy [17].

is shown, in a compilation of data from several experiments by Gaisser [17]. This spectrum is quite steep, with the cosmic ray flux falling from one particle per square meter per second for energies of the order of 100 GeV to one particle per square kilometer per century for energies of the order of 10^{20} eV. It follows practically a power law of the form $E^{-\alpha}$, where α is usually referred as the spectral index and is of the order of 3. The spectrum has slight changes in the spectral index, steepening around 3×10^{15} eV and flattening at 3×10^{18} eV. These features in the spectrum are usually referred to as the “knee” and the “ankle”, respectively and were first inferred by Khristiansen et al. (1956) and Linsley (1963), respectively. At the far end of the spectrum ($E > 10^{19}$ eV) the available statistic is low, and this has been for a while a controversial region. The far end of the spectrum and its features will be discussed in further detail below. The increase in the number of events in this region and the cross-calibration between different detection techniques is a major purpose of the Pierre Auger Observatory.

1.1.1 The GZK effect

The GZK effect has been predicted by Greisen [14] and, independently, by Zatsepin and Kuzmin [25]. The effect consists in the degradation of the energy of cosmic rays above a certain energy threshold through their interaction with the Cosmic Microwave Background (CMB) photons. The CMB radiation presents a black body spectrum with an average temperature of 2.73 K and is present throughout the whole Universe with an isotropic distribution. High energy nuclei interact with this radiation and lose energy. The main process for high energy protons is the photopion production. Protons interact with the CMB photons and give a proton plus a pion. The cross section of the reaction rises as the reaction is mediated through the production of a Δ resonance. This effect has an energy threshold of $E \sim 5 \cdot 10^{19}\,\mathrm{eV}$, and imposes a limit on the mean free path of the protons. In case of heavy nuclei a similar scheme applies but the dominant process for energy loss is the photodisintegration with an energy threshold of the order of $E \sim 5 \cdot 10^{18}\,\mathrm{eV/nucleon}$. A GZK horizon can be defined as the maximum distance from which 90% of the particles with a given energy greater than the threshold energy can come.

Photons arriving to the Earth suffer an equivalent effect, but the dominant process is pair production in the interaction with CMB photons, making the sky opaque for photons with an energy greater than $10^{14}\,\mathrm{eV}$. However, the cross-section for this process will decrease with the increase of the photon energy and the universe will become transparent again for much higher energies.

Figure 1.3, from [8], shows the mean free path for both photons and protons as a function of the energy. As discussed, it can be seen that the mean free path of photons drops for energies of $\sim 10^{14}$ eV, starting to rise afterwards. For protons the mean free path drops at an energy of $\sim 10^{20}$ eV reaching a value of 10 Mpc for energies greater than $5 \cdot 10^{21}$ eV.

1.2 γ rays

The spectrum of diffuse extragalactic photon radiation [21] is presented in figure 1.4 . The energies in the plot range from 10^{-8} eV (radio) to 10^{20} eV. The flux is dominated by the CMB in the microwave region and falls quite rapidly afterwards. For energies above the GeV limits are shown for the γ-ray component. The cosmic ray flux is plotted with open circles for reference.

At such energies the γ-ray diffuse flux is very low and γ-rays are studied by looking at point sources, opening the field of γ-ray astronomy. The first source to be discovered was the Crab nebula. Crab is still the brightest steady emitter for Very High Energy (VHE) γ-rays and is used as a calibration candle. Its spectrum [6], shown in figure 1.5 , extends to several tens of TeV.

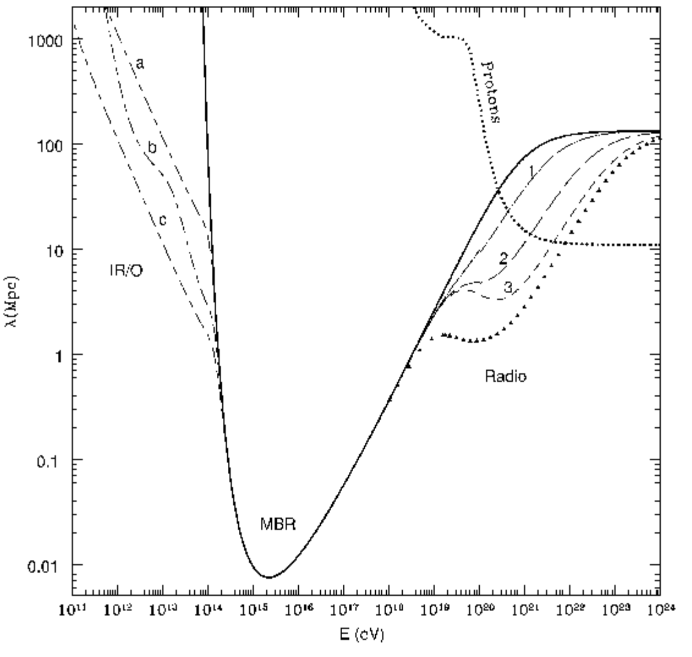

Figure 1.3: Mean free path, λ, of photons and protons as a function of the energy [8]. Photons below 10^{14} eV interact with the Infra-Red and Optical background. Curves a, b and c represent different models of such background radiation; Between $10^{14} - 10^{19}$ eV photons interact with the Microwave Background Radiation. For higher energies the photons interact with radio and the different curves in the plot represent λ under several radio background estimations.

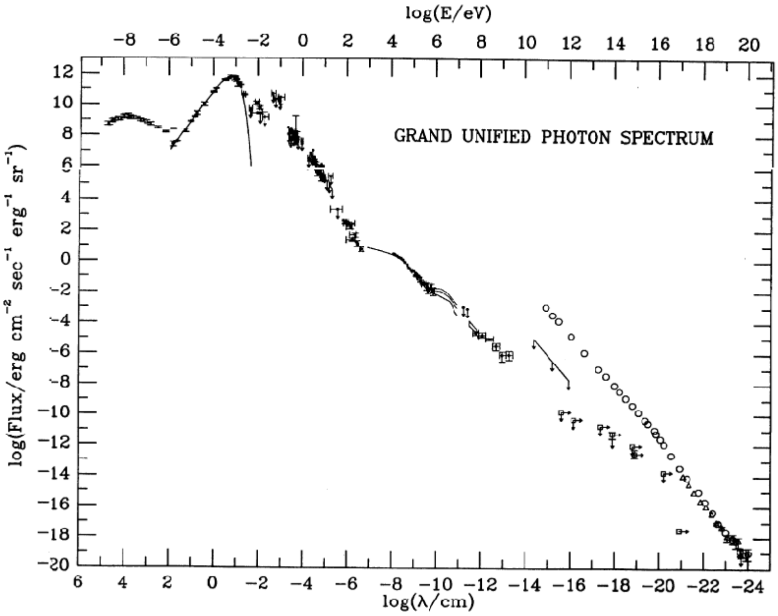

Figure 1.4: The spectrum of diffuse extragalactic photons[21]. For Above GeV energies limits are shown for the γ-ray component. The cosmic ray flux is plotted with open circles for reference.

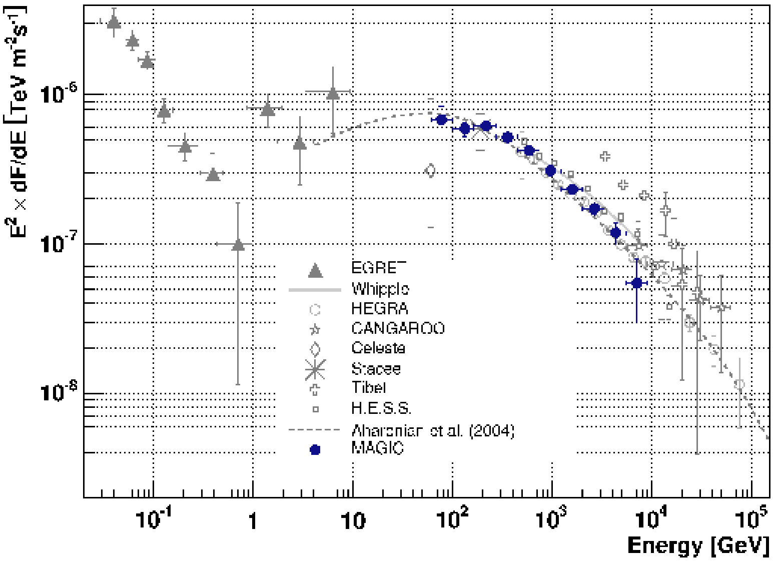

Figure 1.5: The crab γ ray spectrum.

1.3 Extensive Air Showers

It has been known for quite some time that most primary cosmic rays are protons or heavier nuclei. When these high energy particles enter the Earth's atmosphere they interact with the nuclei of atmospheric gases and new particles are created from this interaction. These secondary particles will in turn interact and produce a new generation of particles. In this way the primary particle gives birth to a particle cascade. Such cascades develop in the atmosphere as a front of particles propagating at nearly the speed of light and are commonly known as Extensive Air Showers (EAS) [22, 20] .

As the primary particle enters the atmosphere and the first interaction occurs, pions are produced (and also, in lower number, kaons and baryons). Neutral pions readily decay into a photon pair. Each photon will then disintegrate through pair production. The positrons and electrons created will in turn produce photons and the process will go on until there is not enough energy for the production of new particles. This chain reaction is known as an electromagnetic cascade. Charged pions have a greater mean lifetime and can interact with nuclei before decaying. There are also other particles created in the cascade that can originate nuclear interactions with the nuclei of atmospheric gases. These nuclear interactions originate the hadron component of the EAS. Charged pions can also decay into muons and neutrinos. The muons created have such energy that in most cases they will neither interact with the atmosphere nor decay while traversing it. They constitute the muonic component of the shower that can be detected at sea level.

Although it is known that the primary cosmic rays are nuclei, their exact nature is still a point of controversy. For low energy ($E \lesssim 100$ TeV) particles the detection can be performed directly and the composition of cosmic rays is well known. For higher energies ($E \gtrsim 100$ TeV) the detection relies in indirect methods where the estimation of the primary properties requires the use of interaction models and Monte Carlo (MC) simulations.

1.3.1 EAS simulation

The analytical treatment of the development of air showers is a complex task, viable in practical terms only with many approximations and simplifications. Monte Carlo simulations are in practice the standard method to calculate the properties of EAS. These MC codes start with the primary particle and simulate the interactions of subsequent particles along the shower development in the atmosphere. Two of the main simulation codes are CORSIKA and AIRES. These codes simulate the interactions using different interaction models and follow the particles trajectories in 3D. Such computations for high energies are extremely time consuming, even with state of the art computers. One of the methods for reducing the computing time at high primary energies is the so called thinning method. In this method, below a certain energy only a small fraction of the particles are fully tracked, and they are given a weight to represent the remaining particles. Other simulation codes like CONEX and SENECA take a different approach. In these codes, the particles above an energy threshold are followed explicitly. The numerical description of sub-cascades, initiated by lower energetic particles, is performed using the the solution of cascade equations, reducing the required computation time. [7, 10]

1.3.2 Longitudinal profile

During EAS development particles are created and destroyed. Each particle interacts or decays, giving birth to other particles, each with a fraction of its energy. In this way the number of particles increases. However, low energy particles are easily absorbed in the medium. The number of particles in each step of the cascade will thus be a balance between the creation and annihilation of particles.

Greisen introduced in [12] a parametrization for the total number of electrons in a pure electromagnetic shower initiated by a photon. The shower longitudinal development can be written as a function of the atmospheric depth X as

$$N_e = \frac{0.31}{\sqrt{\beta_0}} \cdot e^{X/\lambda(1-3/2 \ln s)}$$

where $\beta_0 = E_0/\varepsilon_0$, E_0 is the primary energy, ε_0 the critical energy and λ is a characteristic length parameter ($\sim 60 - 70\,\mathrm{g \cdot cm^{-2}}$). The shower age s can be written as:

$$s = \frac{3X}{X + 2X_{\max}}$$

where $X_{\max}$ is the depth of the shower maximum - the atmospheric depth at which the shower contains the maximum number of particles. The shower age parameter is 0 for the first interaction point and is 1 at the shower maximum. At $s = 2$ the shower has already died, with N_e evaluating to less than 1.

Gaisser and Hillas presented in [11] (see also [20]) a parametrization of the average number of particles, N, for hadronic showers with a primary energy E_0. It can be written as

$$N = S_0 \frac{E_0}{\epsilon} \cdot e^{t_m} \left(\frac{t}{t_m} \right)^{t_m} e^{-t}$$

where $S_0 = 0.045$, $\epsilon = 0.074\,\mathrm{GeV}$, $t = {}^{X}\!/\!_{\lambda}$, λ is a characteristic length parameter ($\sim 60 - 70\,\mathrm{g \cdot cm^{-2}}$) and t_m is the depth of shower maximum in units of radiation length. t_m is expressed as

$$t_m = \frac{X_m}{\lambda} = \frac{X_0^{'}}{\lambda} \ln \left(\frac{E_0}{A\epsilon} \right) - 1$$

where A is the atomic number of the nuclei that initiated the shower and $X_0^{'} = 36\,\mathrm{g \cdot cm^{-2}}$. The number of particles at the shower maximum is thus proportional to the primary energy and given by:

$$N_m = S_0 \frac{E_0}{\epsilon}.$$

From the previous formulae it can also be seen that the depth of the shower maximum increases with the logarithm of the energy and, for the same energy, it decreases logarithmically with the nucleus mass A.

A slightly modified parametrization known as Gaisser-Hillas function is currently used to describe and fit the shower longitudinal profile:

$$N(X) = N_{\max} \cdot \left(\frac{X - X_0}{X_{\max} - X_0} \right)^{\frac{X_{\max} - X_0}{\lambda}} \cdot e^{\frac{X_{\max} - X}{\lambda}}$$

where $N_{\max}$ is the number of particles at the shower maximum ($X = X_{\max}$). The parameter X_0 is sometimes referred to as the first interaction point although the fit results for this parameter correlate poorly with the actual depth of the first interaction. Figure 1.6 shows the longitudinal profiles for simulated showers with a primary energy of 10^{19}eV. The profiles for iron-initiated (dashed) and proton-initiated (solid) showers are shown. It can be seen from the figure that while $N_{\max}$ is similar in the two cases, iron-initiated showers have, on average, a lower $X_{\max}$. This earlier development of iron showers is a natural consequence of the fact that the primary energy is carried by the 56 nucleons. Furthermore, it is evident that the fluctuations on $X_{\max}$ are considerable lower for iron-initiated showers. This is due to the fact that each nucleon will interact and produce a sub-shower, reducing the overall fluctuations in the shower. Nevertheless, shower to shower fluctuations are large and make it hard to distinguish, on an event by event basis, a proton shower from an iron shower.

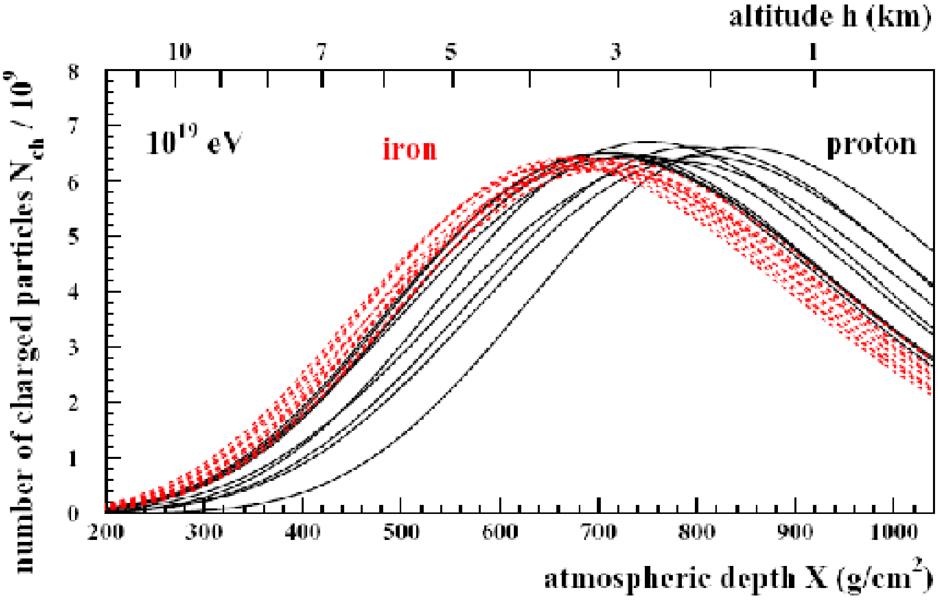

Figure 1.6: Longitudinal profiles for iron and proton initiated showers of energy $E = 10^{19}$ eV.

1.3.3 Lateral profile

In the previous section the longitudinal development of EAS was addressed. Let us now consider the lateral spread of the shower particles. Particles are spread due to multiple Coulomb interactions with the atmospheric nuclei. The cumulative effect of various small-angle scattering interactions builds up the shower transverse structure. The shower can be seen at each instant as a disk, with cylindrical symmetry, which particle density is greater at the center and falls with the disk radius.

The lateral or transverse particle density profile can be parametrised using the Nishimura-Kamata-Greisen function (NKG) [13, 19] that applies to electromagnetic showers:

$$\rho\left(r\right) = c\left(s\right)\frac{N_e}{r_0^2}\left(\frac{r}{r_0}\right)^{s-2}\left(1+\frac{r}{r_0}\right)^{s-4.5}$$

with

$$c\left(s\right) = 0.366 \cdot s^2\left(2.07 - s\right)^{1.25}$$

where s is the shower age parameter and N_e the total number of shower particles. The parameter r_0 is the Molière radius which is defined as $r_0 = \lambda E_s/E_c$ where λ is the radiation length, $E_s \sim 21\,\mathrm{MeV}$ and E_c is the critical energy. In electromagnetic showers, in average, only 10% of the energy lies outside the cylinder with radius R_0.

The lateral distribution function for hadronic showers can be parametrised having as a base the NKG formula. Greisen [13] presents such a parametrization, where a

E	Nb. events	Thin	Wlim
10^5 GeV	100	0	10^4
10^6 GeV	10	10^{-6}	10
10^7 GeV	10	10^{-6}	10^2
10^8 GeV	10	10^{-6}	10^3

Table 1.1: Characteristics of the produced simulation samples. For each energy two samples were generated with different primaries (proton and iron) using the QGSJET hadronic interaction model.

correction factor appears:

$$\rho\left(r\right) = \frac{C_1\left(s\right)N_e}{2\pi r_1^2}\left(\frac{r}{r_1}\right)^{s-2}\left(1+\frac{r}{r_1}\right)^{s-4.5}\left(1+C_2\left(\frac{r}{r_1}\right)^{\delta}\right)$$

The dependence of the transverse distribution with the primary composition and energy was studied with MC simulations in the context of the possibility to use a fluorescence detector with high angular resolution. This study was carried on to investigate the possibility to use such a detector to measure the lateral profile and thus estimate the primary composition.

The transverse momentum distributions of the secondaries produced in an iron-air collision and in a proton-air collision are not substantially different. However, if the primary has the same energy, the average energy per nucleon is, in the case of an iron collision much smaller ($\sim 1/56$) than in the case of a proton collision. This fact should translate into smaller opening angles of the secondaries for proton initiated air showers and thus into narrower transverse distributions, mainly in the central region of the showers, where the hadronic component is stronger. Statistical fluctuations on the properties of the secondaries from the first reaction are small, as the multiplicity in high energy proton-air collisions is of the order of several tens of particles. However, the magnitude of this effect will depend on the boost and thus on the shower energy.

The CORSIKA [16] simulation package, which is the reference in the field, was used to produce samples of EAS initiated by protons and by iron nuclei with energies ranging from 10^{14} to 10^{17} eV. The QGSJET hadronic interaction model was chosen. For energies above 10^{15}eV the thinning option was used setting the thinning parameter $\varepsilon_{\text{th}} = 10^{-6}$ and applying a weight limit $W_{\text{lim}} = E_{\text{prim}} \cdot \varepsilon_{\text{th}}$, where E_{prim} is the primary energy in GeV. These choices ensure that the fluctuations introduced on the e^+e^- lateral distributions by the thinning are of the order of just a few % for distances to the shower axis below 1000 m. Table 1.1 summarises the characteristics

Observation level	Depth (g/cm^2)
1	100
2	200
3	300
4	400
5	500
6	600
7	700
8	800
9	900
10	1000

Table 1.2: Depths of the chosen observation levels.

of the generated samples. The output of each generated event contains information on its longitudinal profile as well as on several transverse profiles at chosen observation levels placed along the shower axis. Table 1.2 summarises the depths of the chosen observation levels.

The lateral profiles near the shower maximum for a proton (solid) and an iron (dashed) event with energy $E = 10^{15}\,\mathrm{eV}$ are shown in figure 1.7 . This plot confirms that the proton lateral distributions are, in the central region, sharper than the corresponding distributions for iron. In figure 1.8 and 1.9 the longitudinal profile of one proton and one iron event, respectively, with an energy $E = 10^{15}$ eV are shown as an example. In the same figures the contributions for the longitudinal profile from the particles with a transverse distance to the shower axis below and above $R_{\mathrm{cut}} = 50$ m are also shown. It is striking that the ratio between these two contributions is well above 1 in the case of the proton-initiated EAS while it is of the order of 1 in the case of iron-initiated EAS. In order to quantify this effect the Rat variable is defined as

$$\mathrm{Rat} = N_{\mathrm{central}}/N_{\mathrm{total}}$$

with

$$N_{\mathrm{central}} = \int_{X_{\mathrm{max}}-\delta}^{X_{\mathrm{max}}+\delta} \int_{0}^{R_{\mathrm{cut}}} \rho\left(r,t\right) drdt$$

$$N_{\mathrm{total}} = \int_{X_{\mathrm{max}}-\delta}^{X_{\mathrm{max}}+\delta} \int_{0}^{\infty} \rho\left(r,t\right) drdt$$

where $\delta = 100\ \mathrm{g}\cdot\mathrm{cm}^{-2}$ and $\rho\left(r,t\right)$ is the particle density at a given distance r

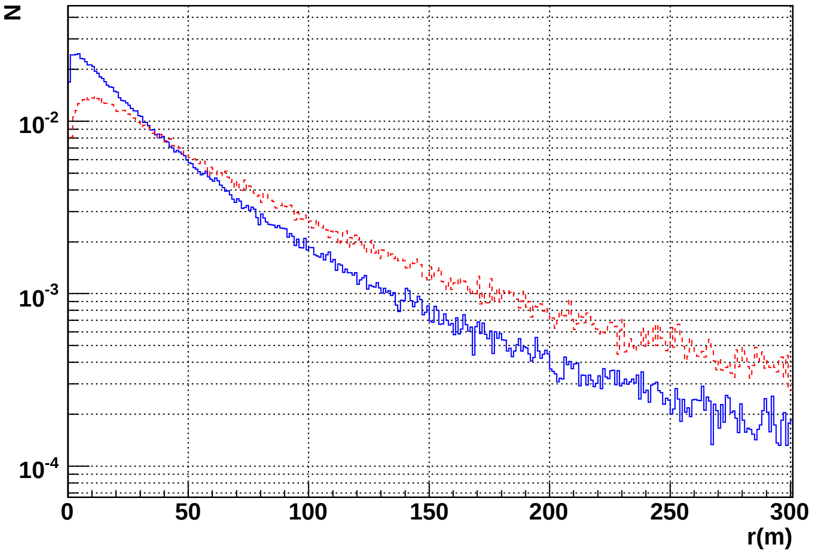

Figure 1.7: Comparison of lateral profiles for a proton (solid blue line) and an iron (dashed red line) event with energy $E = 10^{15}$ eV near the shower maximum. The lateral profiles were taken from the observation level nearest to the shower maximum. In this case the chosen observation levels had a depth of 400 g/cm^2 for iron and 500 g/cm^2 for proton.

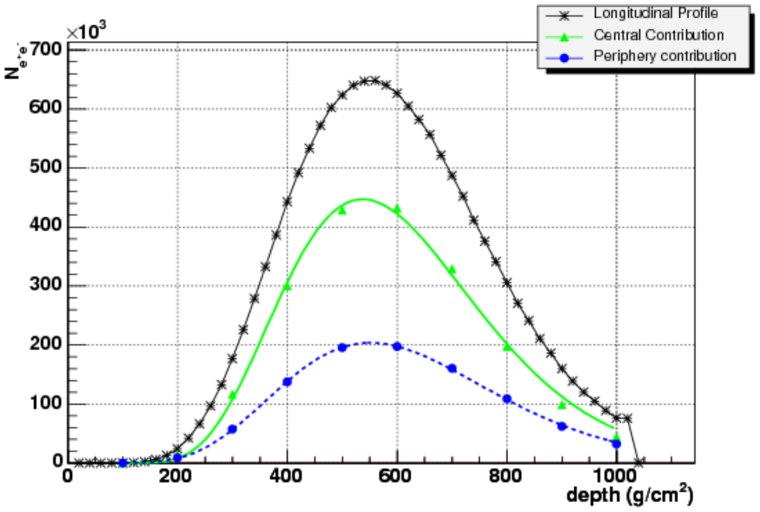

Figure 1.8: Longitudinal profile of a proton event with energy $E = 10^{15}$eV. The total shower profile is shown, together with the separate contributions of the particles at a distance above and below 50 m from the shower axis.

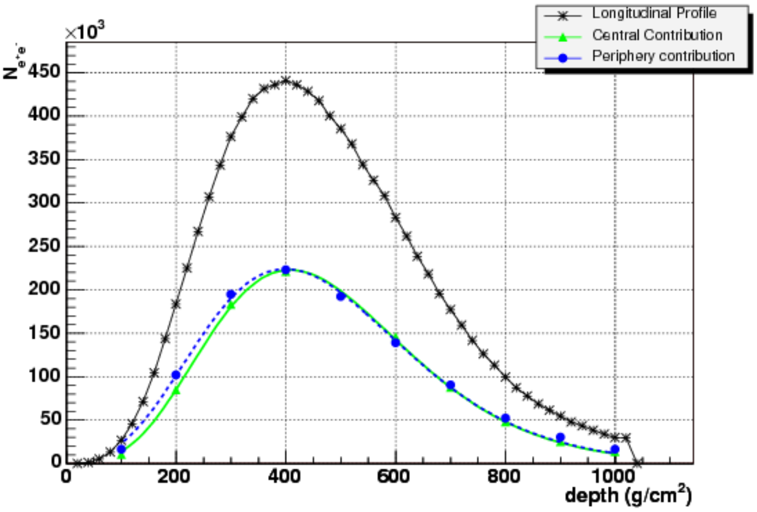

Figure 1.9: Longitudinal profile of an iron event with energy $E = 10^{15}$ eV. The total shower profile is shown, together with the separate contributions of the particles at a distance above and below 50 m from the shower axis.

from the shower axis for a given depth t. Figure 1.10 and figure 1.11 show the distributions of $\mathrm{Rat}_{\mathrm{proton}}$ (solid) and $\mathrm{Rat}_{\mathrm{iron}}$ (dashed) for energies of $E = 10^{14}$ eV and $E = 10^{17}$ eV, respectively. These Rat distributions were computed for two generated samples of proton and iron EAS, with $R_{\mathrm{cut}} = 50$ m. Figure 1.10 shows a clear separation between the Rat distributions for proton and iron initiated EAS. For higher energies the fluctuations in Rat tend to decrease, decreasing the width of the distribution, as can be seen in figure 1.11. It can also be seen that the difference between the proton and iron distributions tend to vanish with the increase of the energy.

In fact, it has been shown in [15] that at high energies ($\sim 10^{19}$ eV) an universal curve can be used for the description of the lateral profile. In this reference CORSIKA simulations were used to study the fluorescence emission through the energy deposited in the atmosphere by the cascade. They conclude that the energy density depends only on the distance to the shower axis and on the shower age parameter. It is independent from the primary energy, composition and zenith angle. A parametrization of the form:

$$F\left(\frac{r}{r_M}\right) = 1 - \left(1 + a\left(s\right)\frac{r}{r_M}\right)^{-b(s)}$$

is presented, where a and b depend only on the age parameter s. The parameters

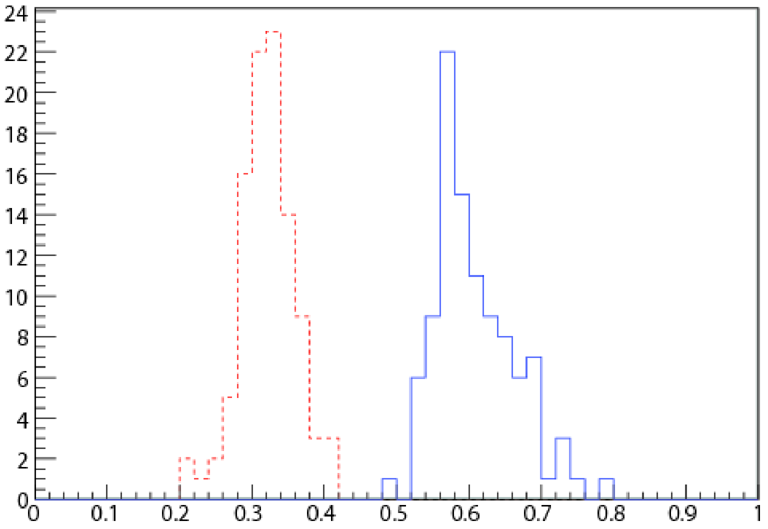

Figure 1.10: Distributions of the Rat variable, defined in the text, for proton (solid) and iron (dashed) EAS generated with an energy of $E = 10^{14}$ eV. For each shower the distribution of particles results from the average of the data between the two observation levels nearest to the shower maximum.

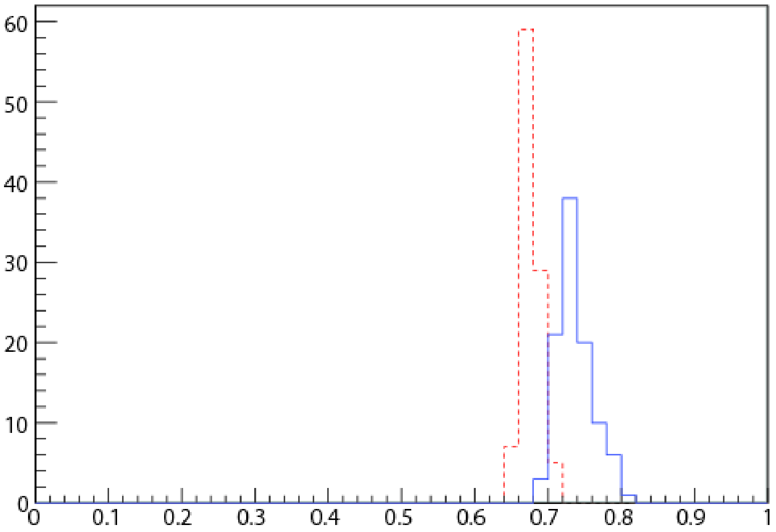

Figure 1.11: Rat distributions for proton (solid) and iron (dashed) EAS generated with an energy of $E = 10^{17}$ eV. For each shower the distribution of particles results from the average of the data between the two observation levels nearest to the shower maximum.

were fitted to the simulation results with polynomials:

$$a\left(s\right) = 5.151s^4 - 28.925s^3 + 60.056s^2 - 56.718s + 22.331.$$

This function is now commonly used in the Auger project to simulate and fit the lateral profile of showers in the fluorescence detector.

1.4 Detection techniques

Cosmic rays can be directly detected at the top of the atmosphere in experiments carried out in balloons or satellites. However the limited aperture of such experiments combined with the rapid decrease of the cosmic ray flux with the energy makes this technique only possible for energies below 10^{14} eV. At higher energies cosmic rays must be studied through the detection of EAS. For this purpose two basic types of detectors are currently used: the ground arrays, based on the sampling technique, and the fluorescence telescopes.

In γ-ray astronomy the fluxes are very much lower than the charged cosmic ray flux. This means that the energy at which ground-based experiments have to be replaced by space-based ones is also lower. For energies up to tens of GeV the detection is space-based, and the most recent and promising experiment is the Gamma-ray Large Area Space Telescope (GLAST[1]) [1] which was recently successfully launched. For higher energies the detection of γ-rays must rely on the detection of EAS. However at these energies the showers do not penetrate deeply in the atmosphere and the most effective instrument for their detection is the Imaging Atmospheric Cherenkov Telescope (IACT), which relies on the detection of the collimated Cherenkov light emitted mainly by the electrons and positrons of the shower in the atmosphere.

1.4.1 Ground arrays

The principle of ground arrays consists of sampling at ground the particle density of the EAS front in order to estimated the primary direction and energy. Ground arrays are composed by a grid of particle detectors. When the shower front crosses one of these detectors, a signal is recorded. This signal is proportional to the local density of particles in the shower front. Mainly two types of detectors are used: scintillators, like in AGASA, and water tanks, like in the Pierre Auger Observatory.

---

[1] NASA announced on 26/08/08 that GLAST has been renamed the Fermi Gamma-ray Space Telescope.

The most widely used scintillators are made of a plastic doped with a scintillating substance. Charged particles deposit energy by ionization and light is emitted by scintillation with an intensity proportional to the deposited energy. Blocks of scintillator are placed in a housing structure along with PMTs. This structure isolates the detector from the outside and directs the light produced to the light sensor (PMT or similar) where it is detected.

In water tanks Cherenkov light is emitted by relativistic particles crossing the detector. The emitted light, basically proportional to the the track length in the water, is reflected in the container walls and recorded using a PMT.

The shower front reaching the detectors is mainly composed by photons, muons and electrons and positrons. Muons penetrate deeply, depositing much less energy by ionization than electrons and positrons. On the other hand, muons cross the water tanks completely, while electrons and positrons are quickly absorbed. This makes water Cherenkov detectors more sensitive to the muonic component of the EAS and scintillators more sensitive to the electromagnetic component.

In both types of detectors the muon flux at the detection level is used to calibrate the detector. The single particle signal is extracted and later used to estimate the number of particles hitting the detector.

The shower front arrival time is recorded at each station with great precision. Assuming that the shower front propagates at the speed of light, the primary direction can be estimated from the time delays in different stations.

The shower size is inferred assuming a lateral shower profile and using it to fit the data from the different stations with signal. The core location is one of the fit parameters and is thus evaluated in the fit. The energy is usually estimated from the density at a fixed distance of the core, extrapolated from the fit. Using extensive Monte Carlo simulations the correlation of this parameter with the primary energy is assessed. The distance at which the density is taken depends on the detector properties, namely the geometry, and is chosen, through MC, as the point where the fluctuations are minimised. For instance AGASA used the density at 600m from the core, while in the Pierre Auger Observatory, where the detectors are farther away, the signal at 1000 m, $S\,(1000)$, is used.

1.4.2 Fluorescence telescopes

In the fluorescence technique Earth's atmosphere is used as a calorimeter to study the primary cosmic rays properties. EAS develop in the atmosphere exciting the air molecules. When the molecules, mainly nitrogen, return to their ground state they emit fluorescence light in the UV, which is detected by means of UV telescopes. Several optics design schemes can be used to build the telescope, but all rely on the use of a large mirror to collect the light and focus it on a PMT camera. Most telescopes are designed to cover a limited field of view and a greater area of the sky is observed by using more than one telescope.

As the atmosphere is used as a calorimeter, a detailed knowledge of its conditions is essential, as the light production and attenuation is related directly to atmospheric parameters. Several atmospheric sensing devices are installed on the Auger site. Weather stations and atmospheric balloons are used to measure directly the atmospheric temperature and pressure. The optical properties of the atmosphere are determined using LIDARs, that measure the scattering in the atmosphere of laser light. Although simple in principle, the solution of the LIDAR equation is not unique and several approximations and assumptions must be made to extract the atmospheric parameters. The detection by the fluorescence telescopes themselves of the light emitted by additional laser devices placed at known distances and scattered in the atmosphere is also used to infer the transmission properties of the atmosphere. Cloud cameras give information on the cloud coverage, extremely valuable for the shower analysis.

Fluorescence telescopes are calibrated using several light sources. Some of these sources are internal and calibrate only the optics and the PMTs of the telescopes. For the Pierre Auger Observatory, an end-to-end calibration device has been specifically developed, which is placed at the entrance of the diaphragm providing uniform and isotropic illumination in the relevant wavelength band. Pulsed laser beams emitted in the field of view of the telescopes are also used for calibration studies.

At each sampling time the EAS is a disk in space, at a certain distance, and illuminates basically a few side-by-side pixels in the camera of the telescope. The image for all samples taken forms a narrow band of pixels with signal, corresponding to the longitudinal development of the EAS. The reconstruction of the shower can be split into two steps: the geometrical reconstruction and the energy reconstruction. An illustration of the geometry used for the reconstruction of fluorescence events is shown in figure 1.12. The line in the centre of the illuminated pixel band and the detector position define the Shower Detector Plane (SDP), the plane in space which contains the shower axis and the detector. The timing information is used to define the shower core coordinates and the shower direction in the plane. The signal recorded by all the pixels can then be used to reconstruct the primary energy. A longitudinal shower profile shape is assumed (usually a Gaisser-Hillas function) and fitted to the light profile, corrected for the atmospheric effects. The integral

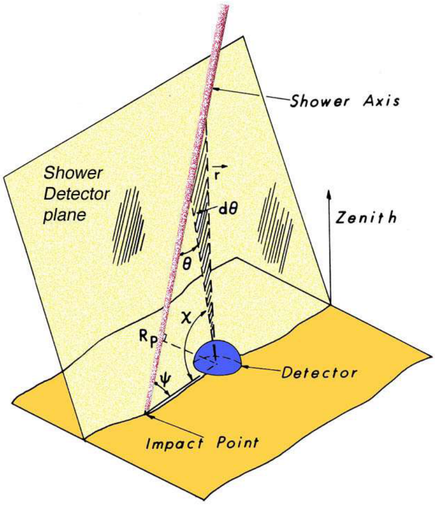

Figure 1.12: Illustration of the geometry used for the reconstruction of fluorescence events.

of the light curve gives an estimation of the energy. This estimation needs to be corrected for the "missing energy" which is the energy carried by particles that do not deposit it in the atmosphere, e.g. the energy carried by the neutrinos, and is usually estimated using Monte-Carlo simulations.

1.4.3 Imaging Atmospheric Cherenkov Telescopes

IACTs are currently the most widely used instruments in γ-astronomy. This technique relies on the detection of the Cherenkov radiation emitted by relativistic EAS particles on the atmosphere. Whereas the particle component does not reach the ground and the fluorescence light is, at the relevant energies, too faint to be detected, the Cherenkov radiation component builds up coherently with the shower front and reaches the ground, where it can be detected.

The detection of cosmic rays using this technique relies on large UV telescopes and arrays of telescopes that are usually characterised by large mirrors and a small field of view ($\sim 5°$).

The telescopes are usually pointed to a known or hypothetical γ-ray source or to specific sky positions as part of a sky survey. If the telescope is inside the Cherenkov pool of light the Cherenkov light is imaged as a filled ellipse in the PMT camera of the telescope. When several telescopes are inside the pool several images are recorded. By analysing the shape and intensity of the signal the parameters of the primary particle are extracted.

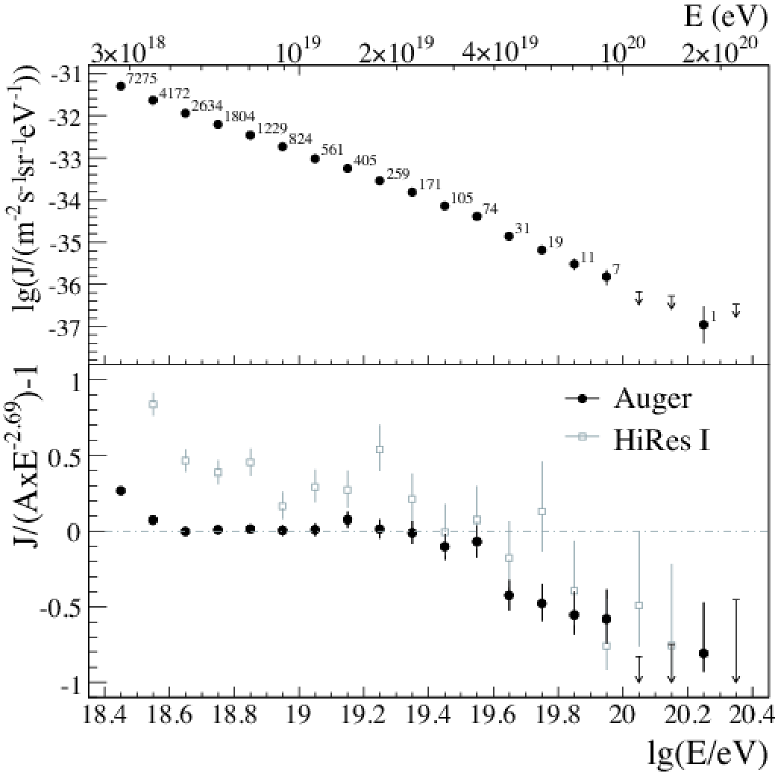

Figure 1.13: The Auger cosmic ray spectrum.

1.5 Recent results

1.5.1 Pierre Auger Observatory results

The first results from the Pierre Auger Observatory include the high energy cosmic ray spectrum, the elongation rate, defined as the variation of the depth of the shower maximum with the logarithm of the energy ($dX_{\max}/d\ln E$), the photon flux and the cosmic rays arrival directions.

Energy spectrum

The cosmic ray energy spectrum measured by the Pierre Auger Observatory was recently published in [5] and is shown in figure 1.13. In the top panel the spectrum is shown, in logarithmic scale, as compiled from 20 000 events recorded by the surface detector. The bottom panel shows the spectrum as the residual from an assumed spectrum with a power law shape of the form $E^{-2.69}$, making its features more evident. These results show that above $4 \cdot 10^{19}$ eV there is a clear change in the spectral index, corresponding to a suppression of the flux. In the figure, data from HiRes I are also presented, also showing a flux suppression in this energy region.

]

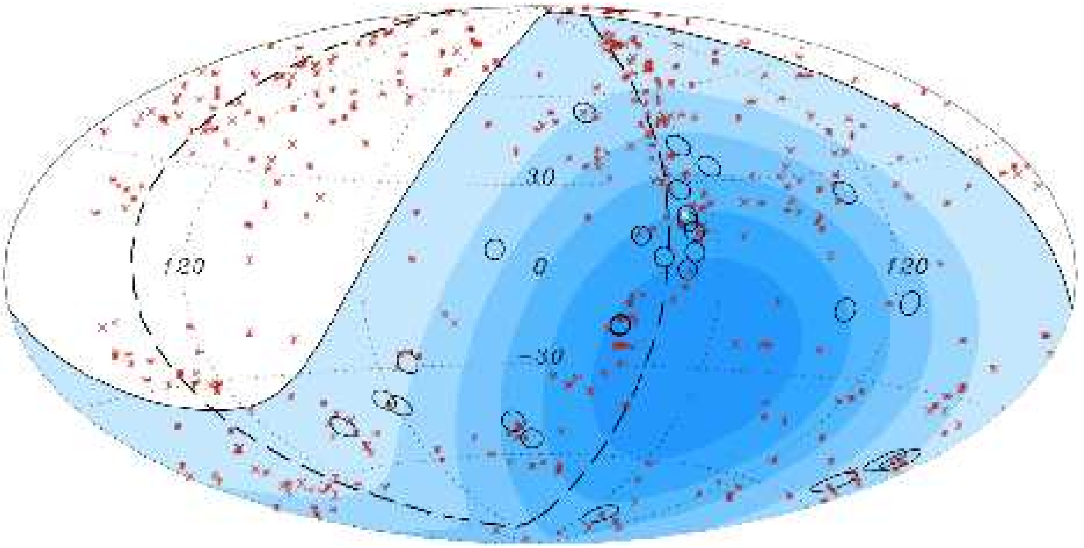

Figure 1.14: The arrival directions of the Auger highest energy events (circles) are shown. The stars represent the positions of nearby AGNs.

These results are compatible with a GZK-like suppression. It is clear that Auger results already represent a great improvement in the precision of the measurement of the spectrum at the highest energies with respect to previous data. Better results are to be expected in the near future, with the increase in the statistics and a better control of the systematic uncertainties. Meanwhile, the understanding of the mass spectrum at the highest energies remains crucial for a full characterisation of the GZK effect.

Arrival directions

The origin of the highest energy cosmic rays remains an open question. In the propagation from the sources to Earth cosmic rays are deflected by magnetic fields. This deflection decreases as the primary energy increases, and increases with the primary charge. The highest energy cosmic rays are expected to point to their sources.

The Pierre Auger Observatory has recently [3] established the anisotropy of the highest energy cosmic rays arrival directions. Figure 1.14 shows the direction in the sky of the highest energy ($E > 57 EeV$) events with circles of 3.1 degrees radius. These parameters result from a scan in the data collected from 1 January 2004 to 26 May 2006 that minimized the probability that the events recorded resulted from an isotropic distribution. A prescription was then established and used to analyse the full data set collected in 3.5 years. The obtained value for the maximum angular distance is compatible with the expectations for the deflections of protons in the magnetic fields. The relative aperture of the detector is indicated by the shading, with the darker zone corresponding to the higher exposure. The dashed line is super galactic plane. The red stars show the positions of nearby AGNs from the 12^{th} Veron-Cetty and Veron catalog (d<75 Mpc, 472 AGNs) [24]. Analyses have been performed searching for correlations of the arrival direction of the most energetic events with different objects, and in particular with AGNs. The figure shows 27 events, 20 of which are correlated with an AGN within 3 degrees. There is evidence for a correlation with AGNs or with objects with a similar distribution. The accumulated statistics is however still relatively low.

Finally, the pointing accuracy indicated by this correlation seems to indicate that the primaries, at these energies, are mainly protons. Such fact might indeed confirm that the observed suppression of the energy spectrum is due to the GZK effect suffered by protons travelling to Earth.

Elongation rate

The shower development in the atmosphere is influenced by the primary composition. Proton primaries will produce longer showers while showers initiated by iron primaries will develop more rapidly for the same primary energy. A method to infer the cosmic ray composition is the study of the elongation rate, that is, the variation of the depth of the shower maximum with the energy ($^{dX_{\max}}/_{d\log E}$).

In figure 1.15, taken from [23], the results from the Pierre Auger Observatory for the average depth of the shower maximum, $\langle X_{\max}\rangle$, as a function of the primary energy are shown. The plot also shows the predictions of different models for iron-initiated and proton-initiated showers. These results show that a single slope would not be sufficient to describe the data, and that the rate of increase of $X_{\max}$ with energy above $E \sim 2 \times 10^{18}\,\mathrm{eV}$ tends to be lower. This seems to indicate a change to lighter primaries up to energies $E \sim 2 \times 10^{18}$ eV and a change to heavier primaries above this energy. More data will however be necessary to establish firmly the high energy behaviour.

This result seems thus in contradiction with the anisotropy results, that indicate proton primaries, and may indicate that the processes involved in the EAS development behave differently from expected. The hadronic interaction models used to simulate EAS are in fact extrapolated from accelerator data to energies several orders of magnitude above, and much is unknown. These results open very interesting particle physics possibilities.

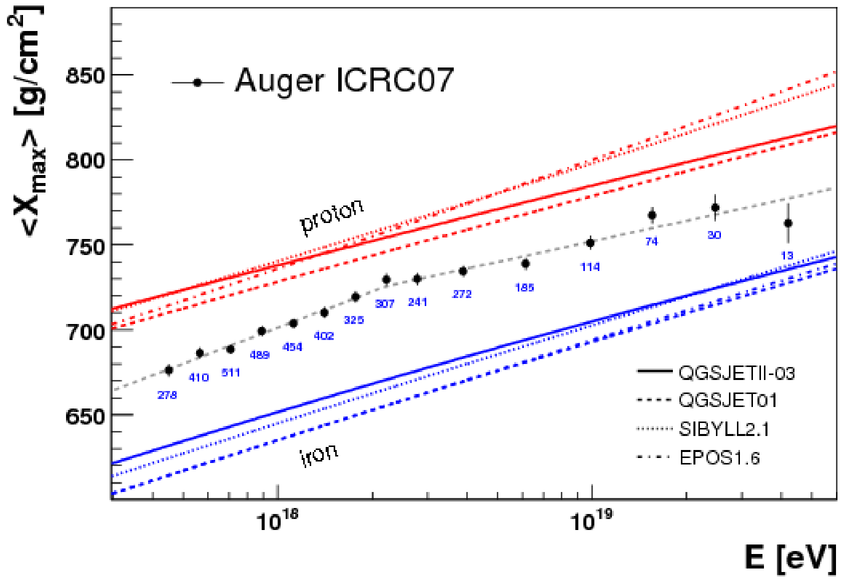

Figure 1.15: The depth of the shower maximum as a function of the energy as measured by Auger is shown and compared with the expectations from different models.

Photon flux

Photon-initiated showers reach the maximum development at much greater depths than proton or iron initiated showers. Using the shower maximum recorded by the Auger fluorescence detector, photon-initiated showers would be distinguishable. The particular characteristics of the development of these shower would also influence the signal recorded by the surface detector of Auger. The shower front curvature and thickness were also used to search for photon shower in the full sample of data.

The data from the Pierre Auger Observatory was searched for photon initiated EAS and no evidence for their observation was found. A limit could then be imposed on the flux of primary photons. These results, presented in [4], are shown in figure 1.16, where the limits on the fraction of photon initiated showers is plotted as a function of the energy along with the predictions of some models. The results from Auger are shown and compared with those from previous experiments. These limits can already exclude most of the top-down models for the creation of high energy photons.

The Pierre Auger Observatory is now fully operational and is expected to collect in one year approximately the same amount of data that was available at the time of the publication of these results. The Pierre Auger results have thus opened a new window for astronomy, astrophysics and particle physics, and very interesting

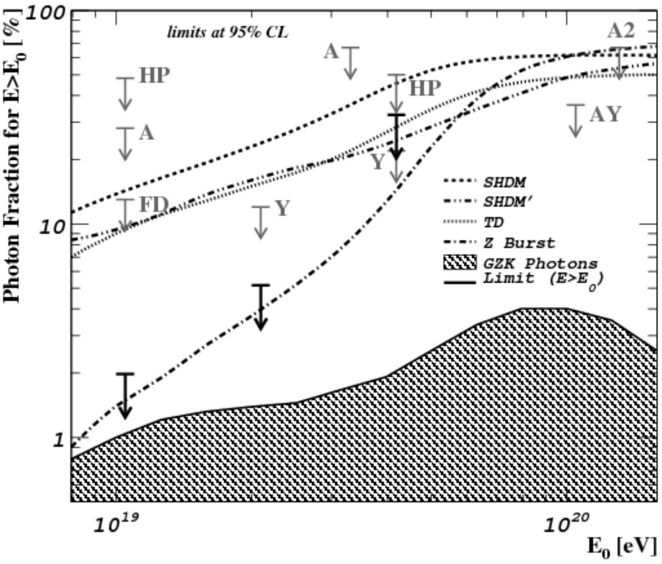

Figure 1.16: Limits on the fraction of photon-initiated showers. The Auger SD (black arrows) and FD limits are shown. For comparison, the predictions of several models and the results from previous experiments are also shown (HP: Haverah Park, A and A2: AGASA, Y: Yakutsk).

results are to be expected soon.

1.5.2 γ-ray astronomy

In recent years the high energy γ-ray field has evolved quite impressively. The advent of new satellite based telescopes like EGRET and AGILE and ground based IACT instruments like MAGIC and HESS allowed the discovery of a large number of sources. A recent and complete review on γ-ray astrophysics can be found in [9]. More than 76 VHE sources have been detected. Their positions are plotted in figure 1.17 . The sources can be identified with several different types of astronomical objects, like Supernova Remnants, Pulsar Wind nebulae and Active Galactic Nuclei. Part of the detected sources is still unidentified. In the figure it is evident that most of the sources lie in the galactic plane. The number of known galactic sources has increased by one order of magnitude in recent years. This comes mainly as a result of a galactic centre survey by the southern hemisphere experiment HESS (see figure 1.18) in the period 2004-2007. The sources accessible from the northern hemisphere were also observed by MAGIC.

The discovery and identification of more sources is to be expected in the near future. GLAST is in orbit since June 2008 and will soon end its commissioning

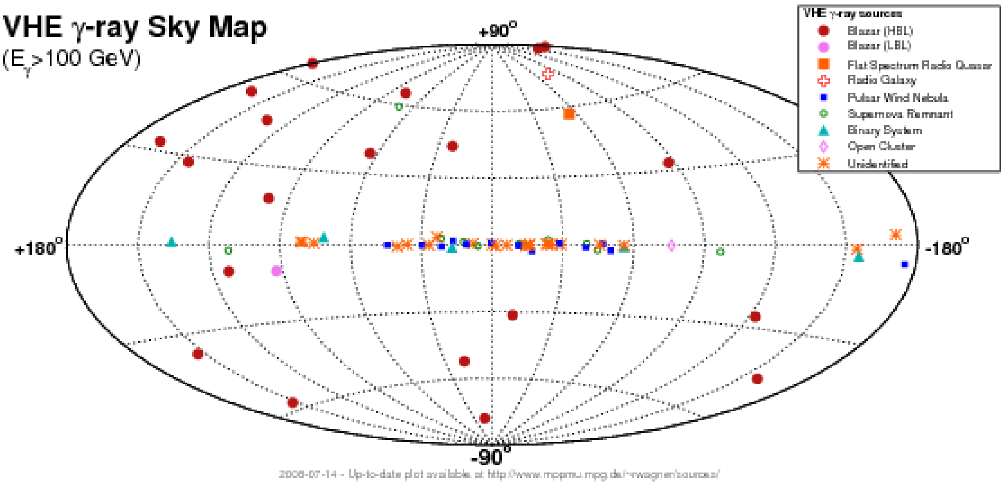

2006-07-14 - Up-to-date plot available at http://www.mppmu.mpg.de/~rwagner/sources/

Figure 1.17: Distribution of the detected VHE γ-ray sources [2].

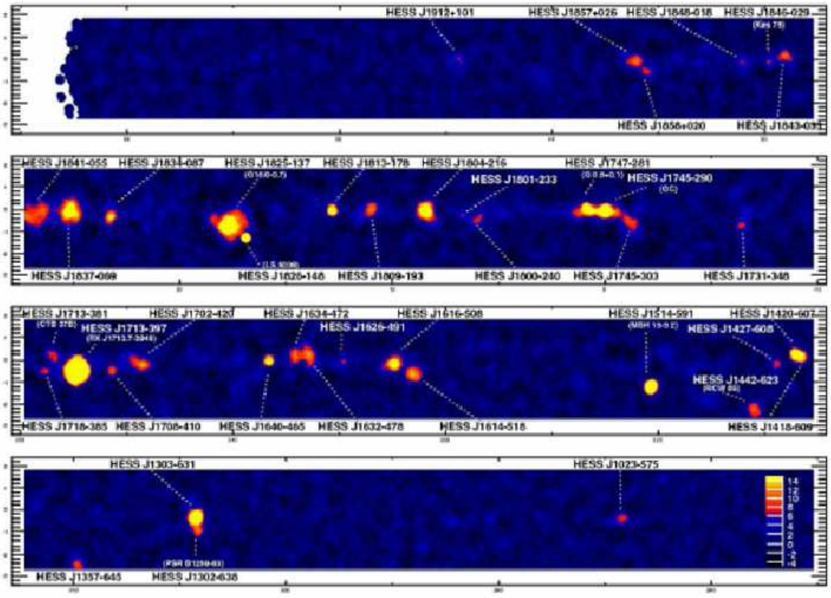

Figure 1.18: γ-ray sources in the galactic plane from the survey performed by H.E.S.S. [18].

Phase, during which some data were already collected. Ground-based detectors should considerably increase the number of identified source as the present detectors are upgraded. MAGIC will move to its phase 2 with the addition of a new telescope, increasing its sensitivity and angular resolution. HESS phase 2 will count with a very large IACT (28 m) installed at the centre of the array and is expected to inaugurate after 2009, reducing the energy threshold and increasing the sensitivity of the experiment.

Bibliography

[1] Official NASA GLAST website at http://glast.gsfc.nasa.gov/.

[2] http://www.mppmu.mpg.de/~rwagner/sources/, 2008.

[3] Abraham, J., et al., Correlation of the highest-energy cosmic rays with nearby extragalactic objects, *Science*, *318*, 938–943, 2007.

[4] Abraham, J., et al., Upper limit on the cosmic-ray photon flux above 10^{19} ev using the surface detector of the pierre auger observatory, *Astroparticle Physics*, *29*, 243–256, 2008.

[5] Abraham, J., et al., Observation of the suppression of the flux of cosmic rays above 4×10^{19}eV, *Physical Review Letters*, *101*, 061,101, 2008.

[6] Albert, J., et al., VHE γ-ray observation of the Crab Nebula and its Pulsar with the MAGIC telescope, *Astrophysical Journal*, *674*, 1037–1055, 2008.

[7] Bergmann, T., R. Engel, D. Heck, N. N. Kalmykov, S. Ostapchenko, T. Pierog, T. Thouw, and K. Werner, One-dimensional hybrid approach to extensive air shower simulation, *Astroparticle Physics*, *26*, 420–432, 2007.

[8] Coppi, P., and F. A. Aharonian, Constraints on the very high energy emissivity of the universe from the diffuse gev gamma-ray background, *Astrophys. J. L.*, *487*, L9–L12, 1997.

[9] De Angelis, A., O. Mansutti, and M. Persic, Very-high energy gamma astrophysics, 2008.

[10] Drescher, H.-J., and G. R. Farrar, Air shower simulations in a hybrid approach using cascade equations, *Phys. Rev. D*, *67*, 116,001, 2003.

[11] Gaisser, T. K., and A. M. Hillas, Reliability of the method of constant intensity cuts for reconstruction of the average development of vertical showers, in *Proceedings of the 15th Int. Cosmic Ray Conf.*, vol. 8, p. 353, Plovdiv, 1977.

[12] Greisen, K., The extensive air showers, *Progress in Cosmic Ray Physics*, *3*, 1, 1952.

[13] Greisen, K., Cosmic ray showers, *Annual Review of Nuclear Science*, *10*, 63–108, 1960.

[14] Greisen, K., End to the cosmic-ray spectrum?, *Phys. Rev. Lett.*, *16*, 748–750, 1966.

[15] Góra, D., R. Engel, D. Heck, P. Homola, H. Klages, J. Pękala, M. Risse, B. Wilczyńska, and H. Wilczyński, Universality of the lateral distribution of energy deposit in extensive air showers, in *Proceedings of the 29th Int. Cosmic Ray Conf.*, vol. 7, pp. 191–194, 2005.

[16] Heck, D., J. Knapp, J. Capdevielle, G. Schatz, and T. Thouw, CORSIKA: A Monte Carlo code to simulate extensive air showers, *Tech. Rep. FZKA 6019*, Forschungszentrum Karlsruhe, 1998.

[17] Hillas, A. M., Cosmic rays: Recent progress and some current questions, *ArXiv Astrophysics e-prints*, 2006.

[18] Hoppe, S., et al., The H.E.S.S. survey of the inner galactic plane, 2007.

[19] Kamata, K., and J. Nishimura, The lateral and the angular structure functions of electron showers, *Progress of Theoretical Physics Supplement*, *6*, 93–155, 1958.

[20] Rao, M. V. S., and B. V. Sreekantan, *Extensive Air Showers*, World Scientific, 1999.

[21] Ressell, M. T., and M. S. Turner, The grand unified photon spectrum: A coherent view of the diffuse extragalactic background radiation, *Comm. on Astrophys.*, *14*, 323, 1990.

[22] Rossi, B., *Cosmic Rays*, McGraw-Hill, 1964.

[23] Unger, M., Study of the cosmic ray composition above 0.4 EeV using the longitudinal profiles of showers observed at the Pierre Auger Observatory, 2007.

[24] Véron-Cetty, M.-P., and P. Véron, A catalogue of quasars and active nuclei: 12th edition, *Astronomy and Astrophysics*, *455*, 773–777, 2006.

[25] Zatsepin, G. T., and V. A. Kuz'min, Upper Limit of the Spectrum of Cosmic Rays, *Soviet Journal of Experimental and Theoretical Physics Letters*, *4*, 78, 1966.